

Hardware-Efficient Large-Scale Universal Linear Transformations for Optical Modes in the Synthetic Time Dimension

Jasvith Raj Basani,^{1,2,*} Chaohan Cui,^{1,3,†} Jack Postlewaite,¹ Edo Waks,^{1,2} and Saikat Guha^{1,3}

¹*Department of Electrical and Computer Engineering,
University of Maryland, College Park, MD 20742, United States*

²*Institute for Research in Electronics and Applied Physics,
and Joint Quantum Institute, University of Maryland, College Park, MD 20742, USA*

³*James C. Wyant College of Optical Sciences, University of Arizona, Tucson, AZ 85721, United States*

Recent progress in photonic information processing has generated strong interest in scalable and dynamically reconfigurable photonic circuitry. Conventional approaches based on spatial interferometer meshes face a fundamental scaling bottleneck, requiring a number of components that grows quadratically with system size. Here, we introduce a hardware-efficient time-domain photonic processor that achieves at least an exponential reduction in component count for implementing arbitrary linear transformations. Our design leverages the favorable scaling properties of the synthetic time dimension by encoding information in time-binned modes and processing them in parallel using recursive switchable short and long-range coupling. The dynamic connectivity of our processor enables systematic pruning of circuit depth, which minimizes optical loss while maintaining all-to-all connectivity. We benchmark our platform on the task of boosted Bell state measurements - a critical component in linear optical quantum computing, and demonstrate that the architecture surpasses the thresholds required for universal cluster-state quantum computation under realistic hardware parameters. We link the performance of our device to the geometric nature of multi-photon transport and show that, contrary to the expectation that redundant faulty hardware degrades performance, localization effects may contribute to improved robustness against coherent errors. Our results establish a practical pathway toward near-term, scalable, and reconfigurable photonic processors for quantum computation and simulation in the synthetic time dimension.

INTRODUCTION

Linear programmable photonic circuits with multiple inputs and outputs are fundamental building blocks in the development of advanced photonic processors, playing a crucial role in both classical and quantum information processing. In the classical regime, such circuits have enabled acceleration of linear algebraic computations, offering significant advantages in machine learning and AI workloads [1–4]. In the quantum domain, their capacity to implement unitary transformations among multiple modes enables high-dimensional quantum logic [5–10], complex control [11–13], and precise long-range interaction of quantized photonic fields [14–16]. This capability underpins quantum-advantageous protocols in photonic quantum computing, communication, and sensing, including boson sampling [17, 18], quantum sensing with dynamic learning [19, 20], and super-additive laser communication systems [21–24].

Traditionally, the most common approach to constructing programmable photonic circuits involves the use of a multi-port interferometer. This approach utilizes a mesh of beam splitters and phase shifters to implement arbitrary unitary transformations [25, 26]. While widely demonstrated, such architectures require

$\mathcal{O}(N^2)$ programmable elements to implement arbitrary unitary operations on N modes, resulting in substantial hardware overhead even on integrated platforms [14–16, 27]. This quadratic scaling imposes substantial overhead, rendering large-scale implementations cumbersome.

In addition to scalability challenges, the reliance on a large number of precision components renders these architectures highly sensitive to fabrication imperfections [28–31]. These imperfections accumulate as the system scales, degrading performance and introducing a challenging trade-off between scalability and achieved fidelity [32–34]. The complexity is further exacerbated when extending such architectures to processors utilizing other optical degrees of freedom, such as time bins. In such cases, the implementation requires an intricate mode sorter with $\mathcal{O}(N)$ phase-stabilized optical paths, which presents formidable practical challenges in large-scale systems.

To address these challenges, alternative architectures that exploit the large-scale multiplexing capabilities of photonics have been proposed [13, 35–37]. In particular, processing information encoded within photonic time bins can significantly reduce the hardware overhead by time-multiplexing the optical components while maintaining full programmability. One

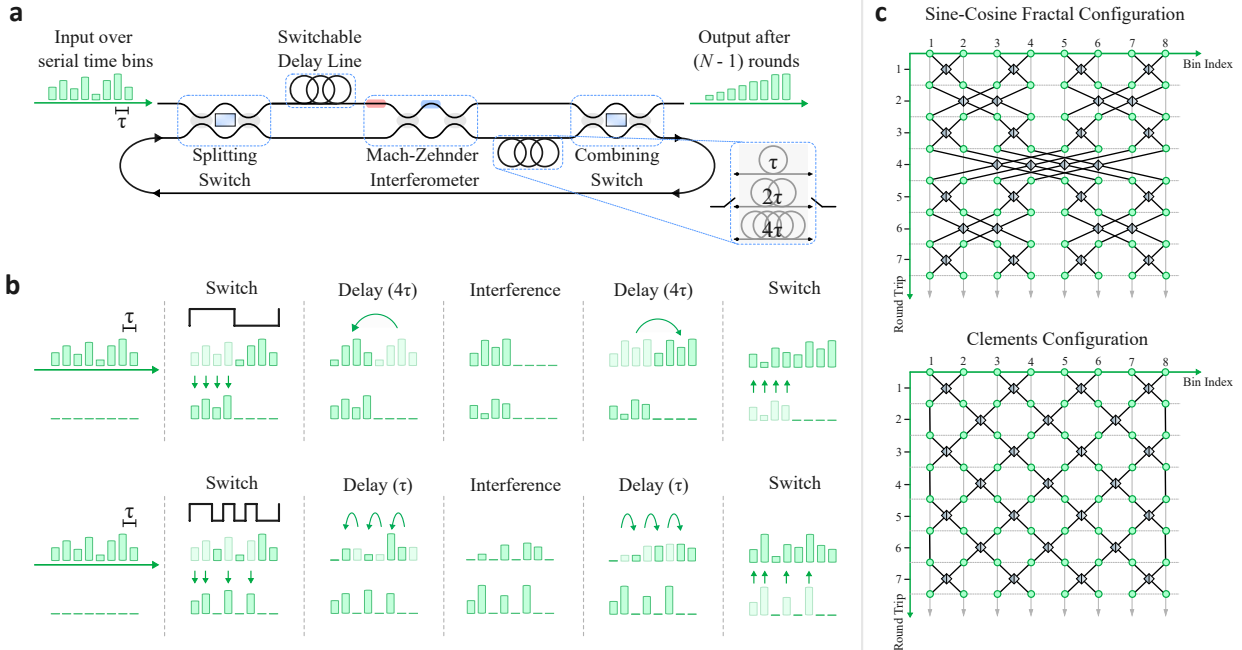


FIG. 1. **Schematic and operation of the generalized Green Machine.** (a) Illustration of the hardware components to construct the generalized Green Machine consisting of switches, delay lines, and programmable beam-splitters. Information is encoded serially over time bins of width τ . (b) Step-wise operations indicating the processes applied to the eight time bins over two spatial modes to interfere with the fourth nearest-neighbor modes. (c) Fully programmable unitary transformations implemented on time-binned modes over multiple round-trips in the Sine-Cosine Fractal configuration and the Clements configuration.

popular approach [38–41] utilizes a pair of short and long optical delay lines requiring $\mathcal{O}(N^2)$ passes through the hardware to construct arbitrary linear transformations. The time cost to compile these matrices scales as $\mathcal{O}(N^3)$. More recently, an alternative approach [42] used optically induced nonlinearities and birefringent materials to perform arbitrary unitary transformations using only $\mathcal{O}(N)$ optical components.

In this manuscript, we introduce the *generalized Green Machine*, a novel time-domain photonic processor for implementing large-scale programmable linear transformations on optical modes encoded in the synthetic time dimension. This recursive architecture significantly reduces the optical hardware required for fully programmable unitary transformations compared to existing approaches, which uses only a single Mach-Zehnder Interferometer (MZI), two switches, and a number of delay lines scaling between $\mathcal{O}(\log_2 N)$ to $\mathcal{O}(1)$, depending on the adopted mesh connectivity.

We provide detailed prescriptions for programming our device to achieve desired unitary matrices and simulate the system’s robustness to imbalanced loss and

coherent beam-splitter errors in the MZI with one-photon and two-photon scattering. After the end-to-end characterization, we benchmark its performance by boosted Bell state measurement [43, 44], a fundamental protocol in linear-optical quantum computation and networking. We show that under practical hardware conditions, our device is capable of surpassing the percolation threshold necessary for universal cluster-state quantum computation [45]. We have further explored that these results are linked to the geometrical nature of our design in multi-photon transport and interference.

PARALLEL INTERFERENCE AND RECURSIVE ARCHITECTURE

The layout of the generalized Green Machine is depicted in Fig. 1(a) as a recursive circuit. This architecture significantly reduces the number of hardware components required to implement arbitrary unitary transformations without affecting the universality. The re-

ursive system comprises a single programmable Mach-Zehnder Interferometer (MZI), two switches, and two optical delay modules. The input photonic state is encoded over complex-valued amplitudes over serialized time bins, with a time interval of τ . The MZI is parameterized by two reprogrammable phases (θ, ϕ) , allowing individual modulation of each time bin. An output port of the second switch is connected to one of the input ports, allowing information to be recursively propagated within this system. This structure enables dynamic programming of connectivity among the time-bin modes, allowing it to be configured into well-established interferometer architectures [25, 26, 46].

To demonstrate the underlying working principle of the generalized Green Machine, we begin with the illustration of the interference performed in a single round-trip. Fig. 1(b) illustrates schematics of step-wise operations applied to 8 time-bin modes to couple fourth-nearest and nearest-neighbor modes. To achieve this function, the first 2×2 optical switch divides the input time bins into two sequences, each directed to a distinct spatial mode, with one sequence leading the other. The leading sequence is then delayed by the appropriate delay line to align with the lagging sequence. When the corresponding pair of time-bin modes arrives, the programmable MZI parameters, θ and ϕ , are set to the values determined by the decomposition of the target unitary operation.

After interference, two output time-bin sequences exit the MZI simultaneously. The delay line in the second arm then delays the output sequence at the bottom port, postponing it after the other sequence in time. At the end of the n^{th} round, the second switch concatenates the two sequences into one. The unitary transformation among the (i, j) time bin modes is written as:

$$U^{(n)}(\vec{\theta}, \vec{\phi}) = \prod T_{i,j}(\theta, \phi), \quad (1)$$

where $T_{i,j}$ is the 2×2 unitary matrix among time bins i and j , parametrized as:

$$T_{i,j}(\theta, \phi) = ie^{i\theta/2} \begin{bmatrix} e^{i\phi} \sin(\theta/2) & \cos(\theta/2) \\ e^{i\phi} \cos(\theta/2) & -\sin(\theta/2) \end{bmatrix}. \quad (2)$$

The output state, after undergoing the unitary transformation $U^{(n)}$ in the n^{th} round, is then fed back into the apparatus for the next round. This process is repeated until the desired global unitary transformation is performed.

By compiling interference patterns in time (via mul-

iple programmed recursive rounds), the generalized Green Machine can be configured to perform arbitrary unitary transformations. The Sine-Cosine Fractal (SCF) architecture [46], shown in Fig. 1(c), is composed of stages with 2^k nearest-neighbor connectivity, where $k \in [0, 1, 2, \dots, N/2]$. To realize the SCF mesh architecture, $\log_2 N$ delay lines of length $2^k \tau$ are sufficient. Alternatively, the device can also be programmed into the Clements architecture [26] by programming alternate stages to couple the nearest-neighbor modes. In this case, a *single* delay line of length τ is sufficient. The stepwise operations, indicating the processes applied to the time-binned modes to configure them into Clements and SCF configurations, are detailed in the Supplementary Information.

PERFORMANCE WITH IMPERFECTIONS

Errors in the generalized Green Machine stem from two main sources. The first arises from component imperfections, which cause the beam-splitters in the MZI to deviate from their ideal 50:50 splitting ratio [28–31, 47]. The second is the imbalanced insertion loss introduced by the switchable delay modules and MZI. We discuss the impact of coherent errors in this section, and the impact of loss in the Appendix.

Imperfect splitting in the beam-splitter ratios, caused by variations in the fabrication process, introduces errors in the programmed unitary matrix. Unlike spatial mode interferometers, the generalized Green Machine utilizes only a single MZI, resulting in correlated errors among all the time-binned modes. Under the influence of these correlated errors, the transfer matrix implemented by the generalized Green Machine U_{GM} deviates from the ideal targeted unitary matrix U_{ideal} . To quantify the impact of these coherent errors, we evaluate the infidelity of a few-photon state $|\psi\rangle$ that is evolved through U_{GM} as:

$$\mathcal{E} = 1 - \mathcal{F} = 1 - \langle \psi | U_{\text{ideal}}^\dagger U_{\text{GM}} | \psi \rangle \quad (3)$$

We evaluate the impact of component imperfections on the Green Machine's ability to implement large-scale unitaries by simulating scattering a single photon across $N_m \in [16, 64, 256]$ time bins. For a given N_m , we sample 10^4 unitaries from the Haar measure, with the beam-splitter error for each circuit (α, β) drawn independently from a Gaussian distribution $\mathcal{N}(0, \sigma)$. Fig. 2(a) illustrates a schematic of an MZI with its splitters perturbed by component errors (α, β) . In fig. 2(b) we plot the state infidelity \mathcal{E} as a function of

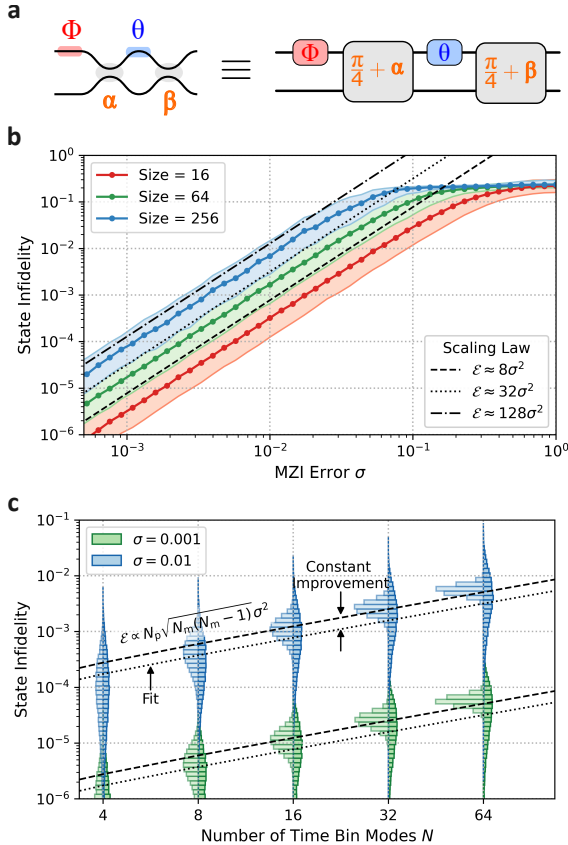


FIG. 2. **Performances of the generalized Green Machine under beamsplitter errors.** (a) Model of MZI with coherent errors (α, β) causing deviations from the ideal 50:50 splitting. (b) State fidelity as a function of beam-splitter errors σ for a single-photon state scattered among $N_m = 256$ time bins. (c) Histograms of the infidelities of the two-photon boson sampling among up to $N_m = 32$ time bins. Infidelities due to the correlated model of errors from the generalized Green Machine are shown in the darker color, fitted with the dotted line. The lighter histograms illustrate the distribution of infidelities under uncorrelated errors (as seen in traditional multiport interferometer architectures), and are fitted with the dashed line.

splitter error σ . The median and interquartile ranges (colored bands) are plotted alongside analytical predictions for spatial-mode interferometers with uncorrelated errors, which scale as $\mathcal{E} \approx \frac{1}{2} N_m \sigma^2$ (black lines; see Appendix). Across all sizes, the Green Machine exhibits lower infidelity, benefiting from its correlated error structure.

An immediate application of large-scale unitaries is boson sampling, which is of interest in quantum computation and simulation. We benchmark the general-

ized Green Machine on sampling an $N_p = 2$ photon state from random unitaries of up to size $N_m = 64$. Fig. 2(c) compares distributions of sampling infidelities for the Green Machine (right) and a conventional spatial mode interferometer (left) with uncorrelated errors under two noise levels: $\sigma = 0.001$ plotted in green and $\sigma = 0.01$ plotted in blue. The dotted and dashed lines are fitted to the median values of these distributions, and follow the scaling law:

$$\mathcal{E} \propto N_p \sqrt{N_m(N_m - 1)} \sigma^2 \quad (4)$$

where the generalized Green Machine shows a constant improvement by a factor of $\sim \sqrt{2}$ for all sizes (see appendix for derivation of coherent errors and imbalanced losses within the MZI).

NEAR TERM APPLICATIONS

Towards Effective Boosted Bell State Measurement

A near-term application that benefits from our architecture is the boosted Bell State Measurement (BSM) [43]. Bell state measurements aim to project the dual-rail-encoded photon pair onto four Bell states: $|\Psi_{\pm}\rangle = \frac{|01\rangle \pm |10\rangle}{\sqrt{2}}$ and $|\Phi_{\pm}\rangle = \frac{|00\rangle \pm |11\rangle}{\sqrt{2}}$, which is a fundamental operation for fusion-based entanglement generations, including quantum teleportation and entanglement swapping [48]. The standard BSM circuit with a single beamsplitter operation can only distinguish between $|\Psi_{\pm}\rangle$ from measurement results, which places an upper bound on the fusion-based entanglement generation success rate at 50% [49]. This success rate can be boosted by incorporating ancillary single-photon modes [43]. An example of such a circuit and its equivalent implementation using three stages of the generalized Green Machine is shown in Fig. 3(a). This circuit increases the BSM success rate to 75% – surpassing the percolation threshold of 67.2% necessary for universal photonic quantum computation with cluster states [45], and increases the efficiency of entanglement generation for quantum networks. An added advantage of using the time-binned architecture is that ancillary single photons can be sequentially generated from a single quantum emitter, which guarantees the indistinguishability required for high-fidelity quantum interference.

The performance of boosted BSM is characterized by two figures of merit: (1) the *success heralding rate*, defined as the probability of heralding the projection into one Bell state according to its detection signature, and

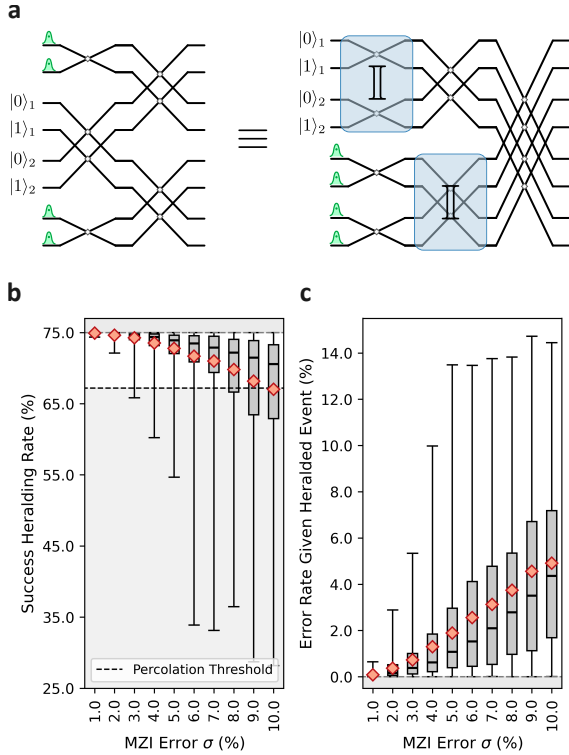


FIG. 3. **Green Machine Implementation of Boosted Bell State Measurement** (a) Circuit of the boosted bell state measurement implemented by 3 stages of the Green Machine to achieve a successful prediction probability of 75%. (b) Probability of successful prediction as a function of beam-splitter error σ . (c) Error given successful prediction as a function of beam-splitter error σ .

(2) the *error rate given heralded event*, which quantifies misidentification rate due to measurement crosstalk after heralding. We employ a Bayesian inference model that assigns posterior probabilities to each detection signature, distinguishing between two outcomes:

- *Decode*, where the event projects the received pattern onto one of the four Bell states if the posterior probability is greater than the decision threshold. This contributes to the success heralding rate. A non-zero probability of detecting the same click patterns by the other Bell states contributes to the increased error rate given this successful prediction.
- *Discard*, where no assignment is made if the posteriors are inconclusive. This results from an inability to decide among the four Bell states, and reduces the heralding success rate.

The success rate predicted by the Bayesian model is subject to variation due to several factors. This includes sources of crosstalk in the time-domain BSM circuit, such as coherent beamsplitter errors, or tunable parameters like circuit depth and decision threshold. Our results are plotted over 1000 samples taken from circuits with emulated noises, as quantile box-plots with the mean value indicated by the red diamond.

First, we evaluate the impact of coherent beamsplitter errors by sampling the splitting errors (α, β) from a normal distribution $\mathcal{N}(0, \sigma)$. Results plotted in Fig. 3(b) and 3(c) illustrate a significant drop in the successful prediction rate (and a corresponding increase in the error rate). At a splitter error of $\sigma = 3\%$, the worst-case success rate drops below the percolation threshold required for universal cluster-state quantum computation. The mean success rate hits this threshold at $\sigma \sim 10\%$, where more than a quarter of the sampled circuits fail at a rate below the standard BSM circuit. These results suggest that the proposed circuit is tolerant to coherent beamsplitter errors, which are usually present in experiments.

Subsequently, we vary the circuit depth by adding redundant stages in the configuration of the SCF mesh. Contrary to expectations that deeper, noisier circuits degrade performance, we observe in Fig. 4(a,b) a non-monotonic improvement in both success and error rates. This counterintuitive behavior is linked to coherent multi-photon transport phenomena, which we analyze in the following section. In practice, the three-stage Green Machine may still be the best option, considering the additional loss brought by redundant stages.

Finally, we sweep the decision threshold, which determines the actions performed in our inference model. By reducing this threshold, the successful prediction rate can be increased, at the expense of the error rate shown in Fig. 4(c) and 4(d), which can serve as a tuning knob for globally optimizing the overall performance of fusion-based photonic quantum computing in practice.

Quantum Transport Simulations

The performance of the Green Machine is strongly linked to the geometrical nature of quantum transport through the time-binned modes [50]. An example of this behavior is distinctly visible in our simulations of the boosted BSM in Fig. 4(a), where the success rate

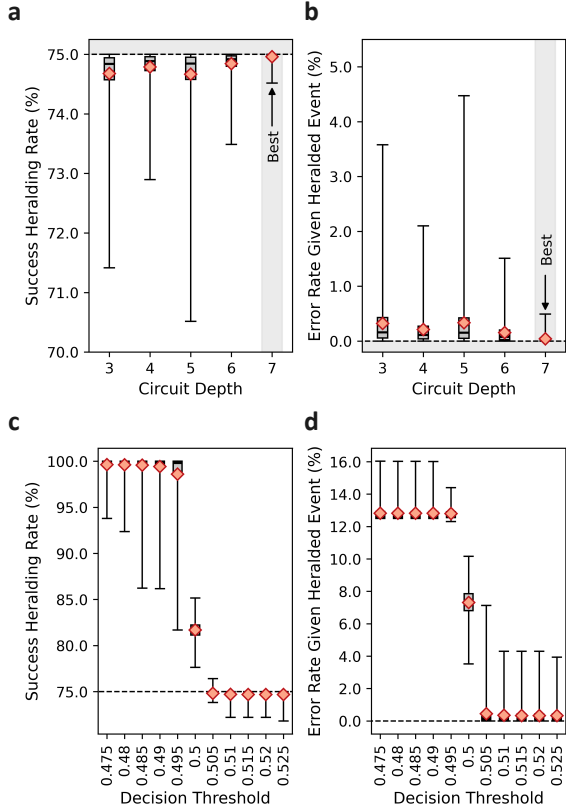


FIG. 4. **Successful heralding rate and error rate given heralded event for boosted Bell state measurement.** Probability of successful heralding and error given heralded event as a function of: (a, b) circuit depth, varying from maximally pruned to fully expressive (c, d) decision threshold with 2% MZI error.

drops at a circuit depth of 5, and increases significantly at a depth of 7. To explain this phenomenon, we study photon transport through the generalized Green Machine when it is configured to the structure of the SCF mesh.

We model this transport by evaluating the evolution of the complex amplitudes of a single-photon state and a bi-photon state after each layer. The initial state is composed of unentangled single photons located at the first (and the second, in the case of two-photon transport) mode(s). This optical state interferes with its 2^n nearest-neighbor modes as it evolves through the stages, with an MZI that is always set to 50:50 splitting before adding random coherent errors. These amplitudes are plotted in Fig. 5 for 8 (similar to the boosted BSM circuit) and 32 time-binned modes.

These simulation results reveal distinct, visually

structured regimes of transport, ranging from fully diffuse to strongly localized. For the case of single-photon transport in an 8-mode system, illustrated in Fig. 5(a), we observe a fully diffuse regime at stage 5, where the probability of detecting the photon is uniformly distributed across all modes. In contrast, at stage 7, the optical state becomes highly localized, with significant amplitude confined to just two modes. This alternating behavior between delocalized and localized regimes persists in larger systems, such as the 32-mode configuration shown in Fig. 5(b), where the transport patterns reflect the self-similar structure of the SCF mesh.

The effects resulting from this self-similarity also produce distinct regimes in the case of multi-photon transport. As an example, we simulate two-photon transport in a 32-mode system, initializing the first two modes with two indistinguishable single photons. The resulting interference patterns, shown in Fig. 5(c), show pairwise excitations of nearest-neighbor modes, which is characteristic of the Hong-Ou-Mandel effect. Similar to the case of single-photon transport, sharply defined regimes emerge where the probability of detecting two photons is either completely vanishing or localized to adjacent pairs of modes.

The introduction of disorder—particularly static perturbations arising from beam-splitter imperfections—modifies these transport characteristics. This disorder has been shown to cause coherent particles to become exponentially localized – a phenomenon commonly known as Anderson localization [51]. In our system, this corresponds to the exponential localization of the optical mode in its respective time bin. We attribute the non-monotonic behavior of the boosted BSM success rate in Fig. 4(a, b) to such localization effects. Specifically, the robustness observed at stage 7 may stem from localization-induced protection, in contrast to the fragility of the diffuse state at stage 5, as shown in Fig. 5(a). The impact of these localization effects and their ability to protect quantum information from coherent errors remains the subject of our future work.

DISCUSSION AND OUTLOOK

We have presented an architecture for the *generalized Green Machine*, a hardware-efficient, universal time-domain linear optical processor that utilizes dual switches. This architecture is naturally compatible with both Clements [26] and SCF mesh [46], to express arbitrary linear unitary matrices in distinct symmetries

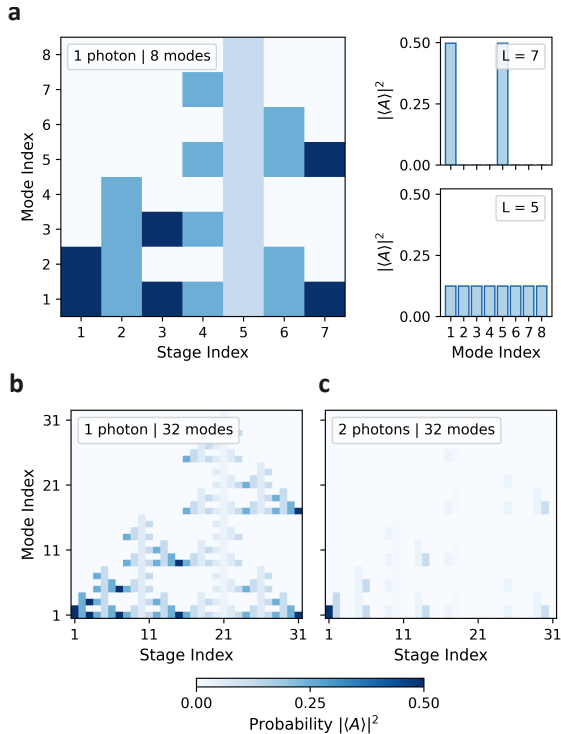


FIG. 5. **Photon transport through the Green Machine.** (a) Single photon transport through the 8-mode circuit, showing a localized state at $L = 7$, and a diffuse state at $L = 5$. (b) Single photon transport with varying degrees of localization in a 32-mode circuit. (c) Two photon transport depicting varying degrees of localization in the presence of Hong-Ou-Mandel interference.

with a minimum number of round trips. We have numerically simulated its performance under practical imperfections on the task of single-photon transportation and Boson sampling, which gains a constant scaling advantage in the average fidelity of targeted unitary circuits.

The two leading figures of merit that can be used to benchmark time-domain optical processors are (1) the hardware complexity, defined as the number of hardware components required to implement an arbitrary $N \times N$ unitary matrix, and (2) the throughput density, defined as the number of multiply-accumulate (MAC) operations per round-trip per amount of hardware required. In terms of hardware complexity, we require at best $\mathcal{O}(1)$ components in the Clements configuration or $\mathcal{O}(\log_2 N)$ components in the SCF configuration, providing at least an exponential reduction in the amount of hardware. Since our device operates on all N modes

in a single round trip, we achieve a linear scaling in throughput density, which is typically realized only with hyper-multiplexing. The comparison with other competing architectures is exhibited in Table I. An additional advantage of the generalized Green Machine is that, since it can be programmed into well-understood interferometric configurations, it is amenable to self-configuration techniques [29, 30, 46], making it more robust to hardware imperfections.

The generalized Green Machine also features flexibility as it allows for systematic reduction of the depth of the linear optical circuit by pruning [46, 52]. Spatial mode linear processors cannot be dynamically pruned – this would involve either bypassing the redundant hardware or physically detaching it. In contrast, the generalized Green Machine allows for pruning by simply reducing the number of recursive rounds. By programming the pruning scheme, the all-to-all connectivity can be maintained while reducing the loss. This is particularly advantageous for implementing classes of transformations with specific symmetries. For instance, achieving an eight-mode boosted Bell state measurement circuit requires only three recursive rounds, while achieving an $N \times N$ Hadamard transform requires only $\log_2 N$ recursive rounds [21]. The proof-of-concept demonstration in a fiber-optical setup has been shown in Ref. [22].

This capability to dynamically program the connectivity, depth, and drop-out ports of the circuit enables the generalized Green Machine to be programmed into fully-general (i.e., non-unitary) beam-splitter meshes [53] such as the diamond [54, 55] or path-independent loss (PILOSS) architectures [56, 57]. Large-scale and high-dimensional transformations can be performed by spatially multiplexing our device. We discuss such a hyper-multiplexed architecture in the appendix, and evaluate the computational speed of such a device for applications such as machine learning accelerators.

In practice, the generalized Green Machine is susceptible to the losses of fast optical switches and optical delay lines. Applications such as boosted Bell state measurement, for instance, would see a sharp drop in fidelity because of such losses. To estimate the amount of loss that can be tolerated, we consider the baseline set by the percolation threshold at 67.2%. Based on estimates from ref. [58, 59], our circuit can tolerate a total of 2 – 3% loss before its performance falls below this threshold. In principle, this requirement may be achieved with fast-developing technology, either through integrated

Architecture	Hardware Complexity	Throughput density [†]
This work	$\mathcal{O}(1)$ or $\mathcal{O}(\log_2 N)$	$\mathcal{O}(N)$
Clements (spatial) [26]	$\mathcal{O}(N^2)$	$\mathcal{O}(1)$
Motes <i>et al.</i> [38]	$\mathcal{O}(1)$	$\mathcal{O}(1)$
Bouchard <i>et al.</i> [42]	$\mathcal{O}(N)$	$\mathcal{O}(N)$

TABLE I. Comparison of hardware complexity and throughput density for approaches to unitary transformations on optical modes. Throughput density[†] in units of MACs/pass/hardware.

photonic technologies [60–62], nonlinear optics [42], or using free-space optics [17, 63] with state-of-the-art single-photon detectors [64].

Data Availability: All requests for code and data should be made to J.R.B. at jasvith@umd.edu.

Code Availability: Source code for the simulations and the accompanying tutorials can be found in the CasOptAx package at <https://github.com/JasvithBasani/CasOptAx>

ACKNOWLEDGEMENTS

All authors acknowledge the DARPA PHENOM project. C.C. and S.G. also acknowledge the DARPA QuANET program for partial support, and thank the support from the Engineering Research Center for Quantum Networks (CQN), awarded by the NSF and DoE under cooperative agreement number 1941583, for synergistic research support.

* These authors contributed equally.

[†] chaohan@umd.edu; These authors contributed equally.

- [1] Y. Shen, N. C. Harris, S. Skirlo, M. Prabhu, T. Baehr-Jones, M. Hochberg, X. Sun, S. Zhao, H. Larochelle, D. Englund, *et al.*, Deep learning with coherent nanophotonic circuits, *Nature Photonics* **11**, 441 (2017).
- [2] S. Bandyopadhyay, A. Sludds, S. Krastanov, R. Hamerly, N. Harris, D. Bunandar, M. Streshinsky, M. Hochberg, and D. Englund, Single-chip photonic deep neural network with forward-only training, *Nature Photonics* **18**, 1335 (2024).
- [3] S. R. Ahmed, R. Baghdadi, M. Bernadskiy, N. Bowman, R. Braid, J. Carr, C. Chen, P. Ciccarella, M. Cole, J. Cooke, *et al.*, Universal photonic artificial intelligence acceleration, *Nature* **640**, 368 (2025).
- [4] S. Hua, E. Divita, S. Yu, B. Peng, C. Roques-Carmes, Z. Su, Z. Chen, Y. Bai, J. Zou, Y. Zhu, *et al.*, An integrated large-scale photonic accelerator with ultralow latency, *Nature* **640**, 361 (2025).
- [5] Y.-H. Luo, H.-S. Zhong, M. Erhard, X.-L. Wang, L.-C. Peng, M. Krenn, X. Jiang, L. Li, N.-L. Liu, C.-Y. Lu, *et al.*, Quantum teleportation in high dimensions, *Physical Review Letters* **123**, 070505 (2019).
- [6] C. Zhang, J. Chen, C. Cui, J. P. Dowling, Z. Ou, and T. Byrnes, Quantum teleportation of photonic qudits using linear optics, *Physical Review A* **100**, 032330 (2019).
- [7] C. Cui, K. P. Seshadreesan, S. Guha, and L. Fan, High-dimensional frequency-encoded quantum information processing with passive photonics and time-resolving detection, *Physical Review Letters* **124**, 190502 (2020).
- [8] Y. Chi, J. Huang, Z. Zhang, J. Mao, Z. Zhou, X. Chen, C. Zhai, J. Bao, T. Dai, H. Yuan, *et al.*, A programmable qudit-based quantum processor, *Nature Communications* **13**, 1166 (2022).
- [9] J. R. Basani, M. Y. Niu, and E. Waks, Universal logical quantum photonic neural network processor via cavity-assisted interactions, arXiv preprint [arXiv:2410.02088](https://arxiv.org/abs/2410.02088) (2024).
- [10] J. Carolan, C. Harrold, C. Sparrow, E. Martín-López, N. J. Russell, J. W. Silverstone, P. J. Shadbolt, N. Matsuda, M. Oguma, M. Itoh, *et al.*, Universal linear optics, *Science* **349**, 711 (2015).
- [11] J. Romero, J. P. Olson, and A. Aspuru-Guzik, Quantum autoencoders for efficient compression of quantum data, *Quantum Science and Technology* **2**, 045001 (2017).
- [12] B. Fischer, M. Chemnitz, B. MacLellan, P. Roztock, R. Helsten, B. Wetz, B. E. Little, S. T. Chu, D. J. Moss, J. Azaña, *et al.*, Autonomous on-chip interferometry for reconfigurable optical waveform generation, *Optica* **8**, 1268 (2021).
- [13] S. Ou, K. Xue, L. Zhou, C. Lee, A. Sludds, R. Hamerly, K. Zhang, H. Feng, R. Koppurapu, E. Zhong, *et al.*, Hypermultiplexed integrated-photonics-based tensor optical processor, arXiv preprint [arXiv:2401.18050](https://arxiv.org/abs/2401.18050) (2024).
- [14] C. Sparrow, E. Martín-López, N. Maraviglia, A. Neville, C. Harrold, J. Carolan, Y. N. Joglekar, T. Hashimoto, N. Matsuda, J. L. O’Brien, *et al.*, Simulating the vibrational quantum dynamics of molecules

- using photonics, *Nature* **557**, 660 (2018).
- [15] X. Qiang, X. Zhou, J. Wang, C. M. Wilkes, T. Loke, S. O'Gara, L. Kling, G. D. Marshall, R. Santagati, T. C. Ralph, *et al.*, Large-scale silicon quantum photonics implementing arbitrary two-qubit processing, *Nature Photonics* **12**, 534 (2018).
- [16] J. Bao, Z. Fu, T. Pramanik, J. Mao, Y. Chi, Y. Cao, C. Zhai, Y. Mao, T. Dai, X. Chen, *et al.*, Very-large-scale integrated quantum graph photonics, *Nature Photonics*, 1 (2023).
- [17] L. S. Madsen, F. Laudenbach, M. F. Askarani, F. Rortais, T. Vincent, J. F. Bulmer, F. M. Miatto, L. Neuhaus, L. G. Helt, M. J. Collins, *et al.*, Quantum computational advantage with a programmable photonic processor, *Nature* **606**, 75 (2022).
- [18] H.-S. Zhong, H. Wang, Y.-H. Deng, M.-C. Chen, L.-C. Peng, Y.-H. Luo, J. Qin, D. Wu, X. Ding, Y. Hu, *et al.*, Quantum computational advantage using photons, *Science* **370**, 1460 (2020).
- [19] Y. Xia, W. Li, Q. Zhuang, and Z. Zhang, Quantum-enhanced data classification with a variational entangled sensor network, *Physical Review X* **11**, 021047 (2021).
- [20] Z.-H. Liu, R. Brunel, E. E. Østergaard, O. Cordero, S. Chen, Y. Wong, J. A. Nielsen, A. B. Bregnsbo, S. Zhou, H.-Y. Huang, *et al.*, Quantum learning advantage on a scalable photonic platform, arXiv preprint [arXiv:2502.07770](https://arxiv.org/abs/2502.07770) (2025).
- [21] S. Guha, Structured optical receivers to attain super-additive capacity and the holevo limit, *Physical Review Letters* **106**, 240502 (2011).
- [22] C. Cui, J. Postlewaite, B. N. Saif, L. Fan, and S. Guha, Superadditive communication with the green machine as a practical demonstration of nonlocality without entanglement, *Nature Communications* **16**, 3760 (2025).
- [23] M. Rosati and A. Solana, Joint-detection learning for optical communication at the quantum limit, *Optica Quantum* **2**, 390 (2024).
- [24] M. Rosati and G. Cincotti, A fourier machine for quantum optical communications, *Journal of Lightwave Technology* (2025).
- [25] M. Reck, A. Zeilinger, H. J. Bernstein, and P. Bertani, Experimental realization of any discrete unitary operator, *Physical Review Letters* **73**, 58 (1994).
- [26] W. R. Clements, P. C. Humphreys, B. J. Metcalf, W. S. Kolthammer, and I. A. Walmsley, Optimal design for universal multiport interferometers, *Optica* **3**, 1460 (2016).
- [27] J. Carolan, M. Mohseni, J. P. Olson, M. Prabhu, C. Chen, D. Bunandar, M. Y. Niu, N. C. Harris, F. N. Wong, M. Hochberg, *et al.*, Variational quantum sampling on a quantum photonic processor, *Nature Physics* **16**, 322 (2020).
- [28] S. Bandyopadhyay, R. Hamerly, and D. Englund, Hardware error correction for programmable photonics, *Optica* **8**, 1247 (2021).
- [29] R. Hamerly, S. Bandyopadhyay, and D. Englund, Accurate self-configuration of rectangular multiport interferometers, *Physical Review Applied* **18**, 024019 (2022).
- [30] R. Hamerly, S. Bandyopadhyay, and D. Englund, Stability of self-configuring large multiport interferometers, *Physical Review Applied* **18**, 024018 (2022).
- [31] R. Hamerly, S. Bandyopadhyay, and D. Englund, Asymptotically fault-tolerant programmable photonics, *Nature Communications* **13**, 6831 (2022).
- [32] R. Burgwal, W. R. Clements, D. H. Smith, J. C. Gates, W. S. Kolthammer, J. J. Renema, and I. A. Walmsley, Using an imperfect photonic network to implement random unitaries, *Optics Express* **25**, 28236 (2017).
- [33] S. P. Kumar, L. Neuhaus, L. G. Helt, H. Qi, B. Morrison, D. H. Mahler, and I. Dhand, Mitigating linear optics imperfections via port allocation and compilation, arXiv preprint [arXiv:2103.03183](https://arxiv.org/abs/2103.03183) (2021).
- [34] J. Ewaniuk, J. Carolan, B. J. Shastri, and N. Rotenberg, Imperfect quantum photonic neural networks, *Advanced Quantum Technologies* **6**, 2200125 (2023).
- [35] R. Hamerly, S. Bandyopadhyay, A. Sludds, Z. Chen, L. Bernstein, S. K. Vadlamani, J. Basani, R. Davis, and D. Englund, Multiplexing methods for scaling up photonic logic, in *AI and Optical Data Sciences IV*, Vol. 12438 (SPIE, 2023) p. 1243802.
- [36] J. R. Basani, M. Heuck, D. R. Englund, and S. Krastanov, All-photonic artificial-neural-network processor via nonlinear optics, *Physical Review Applied* **22**, 014009 (2024).
- [37] R. Hamerly, L. Bernstein, A. Sludds, M. Soljačić, and D. Englund, Large-scale optical neural networks based on photoelectric multiplication, *Physical Review X* **9**, 021032 (2019).
- [38] K. R. Motes, A. Gilchrist, J. P. Dowling, and P. P. Rohde, Scalable boson sampling with time-bin encoding using a loop-based architecture, *Physical Review Letters* **113**, 120501 (2014).
- [39] Y. He, X. Ding, Z.-E. Su, H.-L. Huang, J. Qin, C. Wang, S. Unsleber, C. Chen, H. Wang, Y.-M. He, *et al.*, Time-bin-encoded boson sampling with a single-photon device, *Physical Review Letters* **118**, 190501 (2017).
- [40] S. Sempere-Llagostera, R. Patel, I. Walmsley, and W. Kolthammer, Experimentally finding dense subgraphs using a time-bin encoded gaussian boson sampling device, *Physical Review X* **12**, 031045 (2022).
- [41] M. Monika, F. Nosrati, A. George, S. Sciarra, R. Fazili, A. L. Marques Muniz, A. Bisianov, R. Lo Franco, W. J. Munro, M. Chemnitz, *et al.*, Quantum state processing through controllable synthetic temporal photonic lattices, *Nature Photonics* **19**, 95 (2025).
- [42] F. Bouchard, K. Fenwick, K. Bonsma-Fisher, D. England, P. J. Bustard, K. Heshami, and B. Sussman, Programmable photonic quantum circuits with ultra-fast time-bin encoding, *Physical Review Letters* **133**, 090601 (2024).
- [43] F. Ewert and P. van Loock, 3/4-efficient bell measurement with passive linear optics and unentangled ancillae, *Physical Review Letters* **113**, 140403 (2014).
- [44] N. Hauser, M. J. Bayerbach, S. E. D'Aurelio, R. Weber, M. Santandrea, S. P. Kumar, I. Dhand, and

- S. Barz, Boosted bell-state measurements for photonic quantum computation, *npj Quantum Information* **11**, 41 (2025).
- [45] M. Pant, D. Towsley, D. Englund, and S. Guha, Percolation thresholds for photonic quantum computing, *Nature Communications* **10**, 1070 (2019).
- [46] J. R. Basani, S. K. Vadlamani, S. Bandyopadhyay, D. R. Englund, and R. Hamerly, A self-similar sine-cosine fractal architecture for multiport interferometers, *Nanophotonics* **12**, 975 (2023).
- [47] S. K. Vadlamani, D. Englund, and R. Hamerly, Transferable learning on analog hardware, *Science Advances* **9**, eadh3436 (2023).
- [48] P. Dhara, D. Englund, and S. Guha, Entangling quantum memories via heralded photonic bell measurement, *Physical Review Research* **5**, 033149 (2023).
- [49] J. Calsamiglia and N. Lütkenhaus, Maximum efficiency of a linear-optical bell-state analyzer, *Applied Physics B* **72**, 67 (2001).
- [50] N. C. Harris, G. R. Steinbrecher, M. Prabhu, Y. Lahini, J. Mower, D. Bunandar, C. Chen, F. N. Wong, T. Baehr-Jones, M. Hochberg, *et al.*, Quantum transport simulations in a programmable nanophotonic processor, *Nature Photonics* **11**, 447 (2017).
- [51] P. W. Anderson, Absence of diffusion in certain random lattices, *Physical Review* **109**, 1492 (1958).
- [52] S. Yu and N. Park, Heavy tails and pruning in programmable photonic circuits for universal unitaries, *Nature Communications* **14**, 1853 (2023).
- [53] R. Hamerly, J. R. Basani, A. Sludds, S. K. Vadlamani, and D. Englund, Towards the information-theoretic limit of programmable photonics, arXiv preprint [arXiv:2408.09673](https://arxiv.org/abs/2408.09673) (2024).
- [54] S. Mosca, F. Bilotti, A. Toscano, and L. Vegni, A novel design method for blas matrix beam-forming networks, *IEEE Transactions on Antennas and Propagation* **50**, 225 (2002).
- [55] C. Taballione, T. A. Wolterink, J. Lugani, A. Eckstein, B. A. Bell, R. Grootjans, I. Visscher, D. Geskus, C. G. Roeloffzen, J. J. Renema, *et al.*, 8×8 reconfigurable quantum photonic processor based on silicon nitride waveguides, *Optics Express* **27**, 26842 (2019).
- [56] K. Suzuki, K. Tanizawa, T. Matsukawa, G. Cong, S.-H. Kim, S. Suda, M. Ohno, T. Chiba, H. Tadokoro, M. Yanagihara, *et al.*, Ultra-compact 8×8 strictly-non-blocking si-wire piloss switch, *Optics Express* **22**, 3887 (2014).
- [57] K. Suzuki, R. Konoike, J. Hasegawa, S. Suda, H. Matsuura, K. Ikeda, S. Namiki, and H. Kawashima, Low-insertion-loss and power-efficient 32×32 silicon photonics switch with extremely high- δ silica plc connector, *Journal of Lightwave Technology* **37**, 116 (2019).
- [58] A. Melkozerov, A. Avanesov, I. Dyakonov, and S. Straupe, Analysis of optical loss thresholds in the fusion-based quantum computing architecture, *APL Quantum* **1**, [10.1063/5.0214728](https://doi.org/10.1063/5.0214728) (2024).
- [59] N. Maring, A. Fyrrillas, M. Pont, E. Ivanov, P. Stepanov, N. Margaria, W. Hease, A. Pishchagin, A. Lemaître, I. Sagnes, *et al.*, A versatile single-photon-based quantum computing platform, *Nature Photonics* **18**, 603 (2024).
- [60] L. He, M. Zhang, A. Shams-Ansari, R. Zhu, C. Wang, and L. Marko, Low-loss fiber-to-chip interface for lithium niobate photonic integrated circuits, *Optics Letters* **44**, 2314 (2019).
- [61] L. Chang, M. H. Pfeiffer, N. Volet, M. Zervas, J. D. Peters, C. L. Manganelli, E. J. Stanton, Y. Li, T. J. Kippenberg, and J. E. Bowers, Heterogeneous integration of lithium niobate and silicon nitride waveguides for wafer-scale photonic integrated circuits on silicon, *Optics Letters* **42**, 803 (2017).
- [62] A manufacturable platform for photonic quantum computing, *Nature*, 1 (2025).
- [63] N. T. Arnold, M. Victora, M. E. Goggin, and P. G. Kwiat, Free-space photonic quantum memory, in *Quantum Computing, Communication, and Simulation III*, Vol. 12446 (SPIE, 2023) pp. 25–30.
- [64] D. V. Reddy, R. R. Nerem, S. W. Nam, R. P. Mirin, and V. B. Verma, Superconducting nanowire single-photon detectors with 98% system detection efficiency at 1550 nm, *Optica* **7**, 1649 (2020).
- [65] D. A. Miller, Perfect optics with imperfect components, *Optica* **2**, 747 (2015).
- [66] K. Suzuki, G. Cong, K. Tanizawa, S.-H. Kim, K. Ikeda, S. Namiki, and H. Kawashima, Ultra-high-extinction-ratio 2×2 silicon optical switch with variable splitter, *Optics Express* **23**, 9086 (2015).

SUPPLEMENTARY INFORMATION - HARDWARE-EFFICIENT UNIVERSAL LINEAR TRANSFORMATIONS FOR OPTICAL MODES IN THE SYNTHETIC TIME DIMENSION

Compiling Temporal Mode Transformations

The generalized Green Machine architecture we introduce in the main text compiles transformations stage-wise on time-binned modes to perform a global desired unitary operation. Depending on the pre-programmed configuration being used (Clements, SCF, or otherwise), each stage couples the n^{th} nearest-neighbor modes. In the figure below, we illustrate the step-wise operations indicating the processes being applied to eight time-binned modes. Operations demonstrated in Fig. 6(a, b, c) are sufficient to realize the SCF configuration by coupling fourth-nearest, second-nearest and nearest neighbor modes. Similarly operations in Fig. 6(c, d) are sufficient to realize the Clements configuration by coupling odd and even nearest neighbor modes.

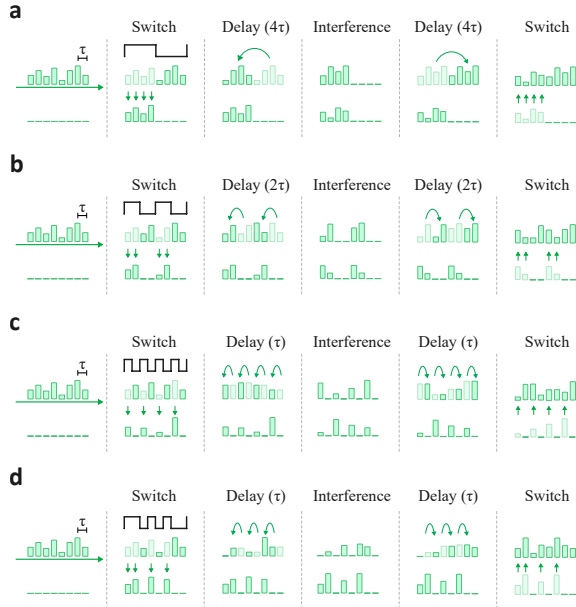


FIG. 6. Step-wise operations to couple n^{th} nearest time-binned modes. Illustration of the switching scheme and the impact of interference on eight time-binned modes. These steps can be used to compile global unitary operations via the SCF configuration using (a, b, c) or the Clements configuration via (c, d).

Derivation of Error Scaling

We are interested in the infidelity of the output state introduced by coherent errors arising from beam-splitter imperfections in unitaries implemented by the generalized Green Machine. Consider a quantum state $|\psi\rangle = \sum c_i \hat{a}_i^\dagger$ that evolves under a unitary implemented by the Green Machine. The notation \hat{a}_i (\hat{a}_i^\dagger) is the annihilation (creation) operator for a bosonic excitation in the i^{th} time bin and c_i is its corresponding probability amplitude such that $\sum |c_i|^2 = 1$.

Under coherent errors introduced by fabrication imperfections, the unitary implemented by the Green Machine U_{GM} deviates from the ideal unitary U_{ideal} as $U_{\text{GM}} = U_{\text{ideal}} + \Delta U$. The fidelity among the ideal output state and the output of the Green Machine is quantified by the expression $\mathcal{F} = \langle \psi | U_{\text{ideal}}^\dagger U_{\text{GM}} | \psi \rangle$ which is bounded $\mathcal{F} \in [0, 1]$.

$$\begin{aligned} \mathcal{F} &= \langle \psi | U_{\text{ideal}}^\dagger U_{\text{GM}} | \psi \rangle \\ &= 1 - \langle \psi | U_{\text{ideal}}^\dagger \Delta U | \psi \rangle \end{aligned} \quad (\text{A.1})$$

To calculate the infidelity $\mathcal{E} = 1 - \mathcal{F}$, we are interested in the effect of the perturbation $\Delta U | \psi \rangle$. The perturbation in the unitary transformation to first order is given by:

$$\Delta U = \sum_n \left[\left(\frac{\partial U}{\partial \alpha_n} \right) \alpha_n + \left(\frac{\partial U}{\partial \beta_n} \right) \beta_n \right] \quad (\text{A.2})$$

At this point, it becomes necessary to introduce an error model. In a general multiport interferometer, beam-splitter imperfections can be assumed to be uncorrelated. This suggests that for a given error amplitude of σ , the deviations $\langle \alpha_n \rangle_{\text{rms}} = \langle \beta_n \rangle_{\text{rms}} = \sigma$. Ref. [30] shows that

$$\left\| \frac{\partial U}{\partial \alpha_n} \right\| = \left\| \frac{\partial U}{\partial \beta_n} \right\| = \sqrt{2} \quad (\text{A.3})$$

Therefore the error measure quantified by the Frobenius norm $\|\Delta U\| \propto \sqrt{2}\sigma$, which is bounded in the interval $[0, 2]$. The infidelity caused by scattering in an interferometer architecture is instead proportional to $\|\Delta U\|^2 = \sum_{i,j} |U_{i,j}|$ and can be calculated from Eq. (A.2) by adding the error terms in quadrature over

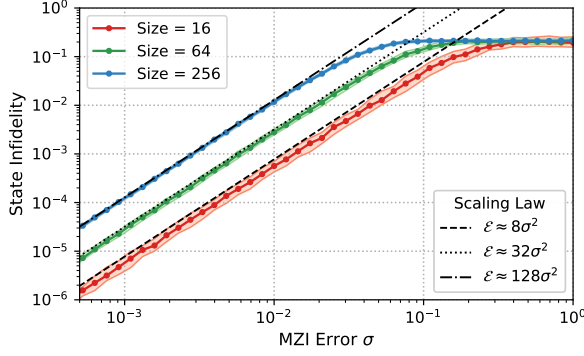


FIG. 7. **Scaling of state infidelity as a function of MZI error.** Numerical simulations and analytically derived scaling for a single photon fock state scattered among upto $N_m = 256$ time bins, with uncorrelated errors. The numerical simulations agree with the analytical solution for large unitaries.

the $N_m \times (N_m - 1)$ splitter to give us:

$$\mathcal{E} = \frac{1}{2} \sqrt{N_m(N_m - 1)} \sigma^2 \approx \frac{1}{2} N_m \sigma^2 \quad (\text{A.4})$$

In the case when $|\psi\rangle$ contains a total of N_p photons, i.e., $|\psi\rangle$ is a normalized superposition of multimode multi-photon states, it is easy to see that the infidelity is linearized in terms of the photon number, given by:

$$\mathcal{E} = \frac{N_p}{2} \sqrt{N_m(N_m - 1)} \sigma^2 \quad (\text{A.5})$$

To verify these expressions, we plot the state infidelity as a function of MZI errors for the case when errors are uncorrelated. Specifically, this reflects the case of

single-photon scattering in a multiport interferometer with uncorrelated errors [28–30, 46]. For large unitaries, the analytical and numerically simulated error scaling are identical. For smaller mesh sizes, the analytical solution begins to deviate from the numerical simulations because the errors do not average out over the ensemble of small numbers of phases.

In the generalized Green Machine, the errors are correlated since only a single MZI is used recursively, i.e., (α, β) are both sampled independently from the distribution $\mathcal{N}(0, \sigma)$. Under this correlated model of errors, the matrix error which depends on $\langle(\alpha + \beta)\rangle_{\text{rms}}$ scales as $\sigma/\sqrt{2}$, giving us at least constant improvement by a factor of $\sqrt{2}$. This improvement in fidelity is seen in Fig. 2 of the main text.

Inaccessible states from intra-MZI imbalance of loss

In practice, the unbalanced transmission coefficients on each arm of the MZI, denoted by (Γ_1, Γ_2) in fig. 8(a), usually result in a drop in the expressivity of a linear optical circuit, which is indicated by the existence of inaccessible output states given all possible input states. These inaccessible output states that arise as a result of coherent errors and unbalanced loss can be determined by evaluating the range of admissible splitting ratios implemented by the end-to-end transfer matrix of our single MZI beamsplitter, akin to the method in Ref. [31]. For a given 2×2 transfer matrix U implemented on a set of time-bin modes, the complex-valued splitting ratio is defined as $s = U_{11}/U_{12}$. The range of admissible splitting ratios in the presence of splitter error (α, β) and unbalanced transmission coefficients (Γ_1, Γ_2) on each arm reduces to:

$$\begin{aligned} \frac{\Gamma_1 [\cos|\alpha - \beta| - \sin|\alpha + \beta|] - \Gamma_2 [\cos|\alpha - \beta| + \sin|\alpha + \beta|]}{\Gamma_1 [\cos|\alpha + \beta| - \sin|\alpha - \beta|] + \Gamma_2 [\cos|\alpha + \beta| + \sin|\alpha - \beta|]} &\leq |s| \\ &\leq \frac{\Gamma_1 [\cos|\alpha - \beta| - \sin|\alpha + \beta|] + \Gamma_2 [\cos|\alpha - \beta| + \sin|\alpha + \beta|]}{\Gamma_1 [\cos|\alpha + \beta| - \sin|\alpha - \beta|] - \Gamma_2 [\cos|\alpha + \beta| + \sin|\alpha - \beta|]} \end{aligned} \quad (\text{A.6})$$

which reduces to $\tan|\alpha + \beta| \leq |s| \leq \cot|\alpha - \beta|$ in the lossless setting [31] and $\frac{\Gamma_1 - \Gamma_2}{\Gamma_1 + \Gamma_2} \leq |s| \leq \frac{\Gamma_1 + \Gamma_2}{\Gamma_1 - \Gamma_2}$ in the absence of coherent errors.

Accessible splitting ratios over a single stage in the presence of these errors can be visualized on a Riemann Sphere, illustrated in Fig. 8. Under purely unbalanced loss where $(\Gamma_1 = 0.5, \Gamma_2 = 0.9)$ chosen for

illustrative purposes), forbidden regions near the poles emerge, indicated in red in Fig. 8(b), showing regions where perfect nulling of the power is impossible. In the presence of both unbalanced loss and coherent errors, the forbidden regions that emerge are asymmetric, given by Eq. (A.6). Fig. 8(c) illustrates this case with $(\alpha = 0.15, \beta = 0.0)$, where the inaccessible region at

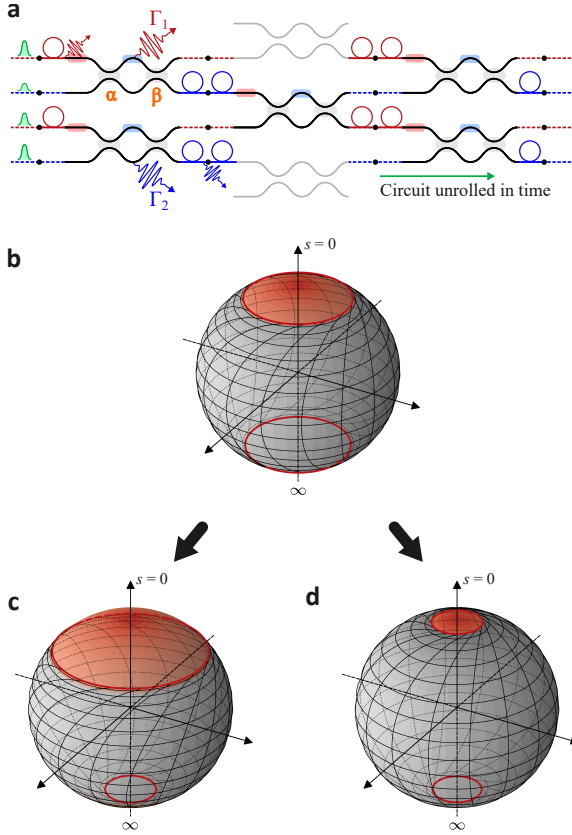


FIG. 8. **An illustration of accessible regions of tunable beamsplitter's splitting ratios restricted by loss and coherent errors.** (a) Circuit implemented by the recursive structure of the Green Machine unrolled in time, identifying the two imbalanced loss factors Γ_1 and Γ_2 taken into account. (b) Riemann sphere representation of accessible splitting ratios, with the forbidden regions shown in red. Purely unbalanced loss (transmission coefficients chosen to be $(\Gamma_1 = 0.5, \Gamma_2 = 0.9)$ for illustrative purposes) introduces forbidden regions around the poles. (c) Coherent errors (chosen to be $(\alpha = 0.15, \beta = 0.0)$) perturb the forbidden regions around the poles asymmetrically, which could happen in spatially-meshed linear optical circuits. (d) Lower degree of imbalance in the loss (transmission coefficients chosen to be $(\Gamma_1 = 0.7, \Gamma_2 = 0.9)$) on each arm shrinks the forbidden regions.

the $s = 0$ pole expands, while the region at the $s = \infty$ pole contracts. This suggests that the forbidden region at one of the poles can be eliminated entirely, allowing

the realization of the perfect cross state for improved matrix fidelity. [31, 65, 66].

When the degree of imbalance in loss on each arm is reduced (i.e., as $\Gamma_1/\Gamma_2 \rightarrow 1$), the inaccessible regions shrink, shown in Fig. 8(d). Perfectly balanced loss eliminates the forbidden regions completely, allowing access to the full range of splitting ratios while resulting in only a scaling down of the output power. Imbalanced loss arising from interfacing each time bin with delay lines asymmetrically *over multiple stages* (such as the Clements configuration shown in fig. 8(a)) cascades into a complex chain of errors, further reducing circuit expressivity.

However, since the generalized Green Machine in Clements mesh only accesses a single MZI repeatedly, the whole circuit performance can be characterized by two coherent-error parameters α and β , two intra-MZI loss parameters Γ_1 and Γ_2 , and two delay line loss rates, which is the subject of our future work.

Large-Scale Multiplexing for Tensor Operations

While the results in this manuscript have mainly focused on applications involving quantum computation, this architecture is also well suited to implement the large-scale and high-dimensional unitaries necessary for machine learning accelerators. A metric commonly used to evaluate the performance of these accelerators is the number of multiply-accumulate operations per second (MACs). Here, we evaluate the computational speed of matrix-vector multiplications implemented by the generalized Green Machine as a function of the width of the time-bins used.

Fig. 9(a) illustrates a schematic for a spatially and temporally multiplexed Green Machine architecture, consisting of multiple stages of the generalized Green Machine introduced in the main text of this manuscript. By stacking M individual stages together, where each stage operated on N time-binned modes, this processor can be used to perform $M \times M \times N$ tensor operations. Fig. 9(b) plots the computational speed of a single stage and the multiplexed stages as a function of the width of the time-bins. We mark the speeds of each architecture using the dotted line at a previous experimental implementation [22] from the authors and state-of-the-art switching speeds [42].

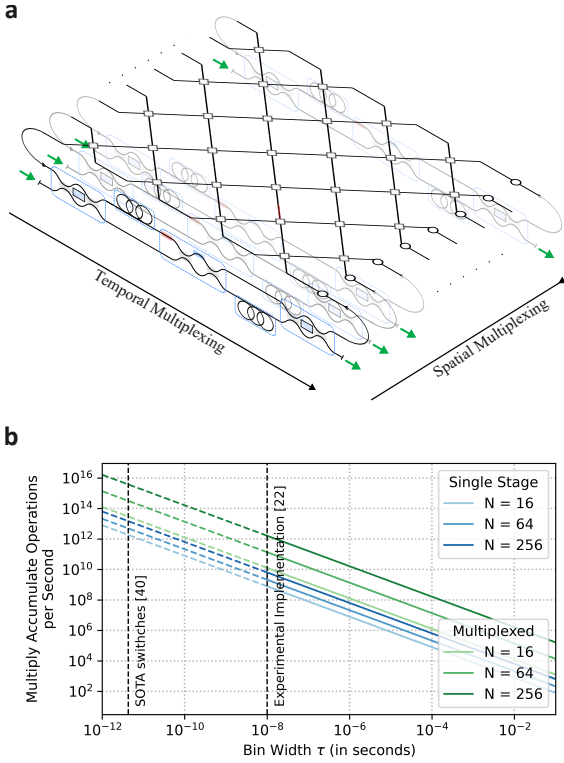


FIG. 9. **Multiplexed architecture and computational speed for high-dimensional tensor operations.** (a) Multiplexed architecture by cascading a single-stage generalized Green Machine for high-dimensional unitary transformations for data encoded in spatial and temporal degrees of freedom. (b) Number of multiply-accumulate operations per second in matrix-vector multiplication as a function of the bin width, as decided by the switching speed. The experimental implementation of the Green Machine is marked in ref. [22] at a bin width of 10 ns. State-of-the-art switching speeds from ref. [42] is marked, at bin widths of ≈ 4.3 ps.